Earth and Planetary Science Letters 426 (2015) 109–117

Contents lists available at ScienceDirect

Earth and Planetary Science Letters

www.elsevier.com/locate/epsl

Seismic evidence for the North China plate underthrusting beneath northeastern Tibet and its implications for plateau growth

Zhuo Ye [a], Rui Gao [a,*], Qiusheng Li [a], Hongshuang Zhang [a], Xuzhang Shen [b], Xuzhou Liu [b], Chen Gong [a]

[a] State Key Laboratory of Continental Tectonics and Dynamics, Key Laboratory of Earthprobe and Geodynamics, MLR, Institute of Geology, Chinese Academy of Geological Sciences, Beijing, 100037, China
[b] Lanzhou Institute of Seismology, China Earthquake Administration, Lanzhou, 730000, China

ARTICLE INFO

Article history:
Received 27 February 2015
Received in revised form 9 June 2015
Accepted 13 June 2015
Available online 2 July 2015
Editor: P. Shearer

Keywords:
northeastern Tibet
North China craton
receiver function imaging
lithospheric structure
underthrusting
plateau growth

ABSTRACT

Lithospheric deformation of the Tibetan plateau is caused by subduction of the Indian (northward) and Asian (southward) plates. The effects of this interaction on inner reaches of the Asian continent, between the Tibetan plateau and the North China craton (NCC) for example, remain uncertain due to poor geophysical data coverage in northeastern Tibet (NE Tibet). We provide here detailed knowledge of the lithospheric structure beneath NE Tibet as determined from a dense broadband seismic profile traversing NE Tibet to the westernmost NCC. Receiver function imaging reveals several significant features, including a north-dipping intracrustal converter (NC), Moho offset/overlap beneath major fault zones, and a low velocity layer (LVL) in the middle-lower crust. The lithosphere–asthenosphere boundary (LAB) is clearly defined and appears as a south-dipping interface that runs continuously from the Alxa interior to the Qilian orogen. Interpretation of these observations, combined with other seismic evidence, implies that the NCC lithospheric mantle has been persistently underthrust beneath the Qilian orogen. This process forms the thick-skinned crustal accretionary wedges, which develop above a middle-lower intracrustal decollement. Our results provide further deep-geophysical constraints on the Cenozoic post-collisional evolution of the convergent boundary between NE Tibet and the NCC and help clarify the mechanism of plateau growth in this boundary area.

1. Introduction

Activation and deformation of the continental lithosphere during Cenozoic collision of the northward-drifting Indian plate and the relatively stationary Asian plate caused formation and growth of the Tibetan plateau. A growing number of seismic observations (e.g., Kind et al., 2002; Nabelek et al., 2009; Zhao et al., 2010, 2011; Zhang et al., 2012b; Yue et al., 2012; Replumaz et al., 2013) have indicated that the post-collisional convergence of India and Asia was accommodated by mantle lithosphere subduction of the Indian plate beneath southern Tibet and the Asian plate component of north–central Tibet, although some studies suggest no south-verging subduction of Eurasian lithosphere (e.g., Ceylan et al., 2012; Liang et al., 2012). Most of these previous seismic profiles did not cover the northeastern margin of the plateau however (i.e., the transition area from the Qilian orogen to the Alxa block), so that the nature of the lithospheric contact between the Tibetan plateau and the North China craton (NCC) in NE Tibet remains obscure.

As the leading edge of the plateau's northeastward expansion, fold and thrust belts in NE Tibet (e.g., Qilian Shan) are currently undergoing shortening/thickening and topographic uplift as they are incorporated into the plateau (Meyer et al., 1998). To understand the tectonic dynamics of convergence between NE Tibet and the NCC, as well as subsequent uplift of this area, we present a comprehensive lithospheric-scale model based on new results and previous profiles, which directly image the lithospheric contact between NE Tibet and the NCC. The images derive from a new, high-quality teleseismic receiver function (RF) dataset from a 550 km profile consisting of 38 densely spaced, broadband seismic stations (Fig. 1). This seismic profile traverses the entirety of NE Tibet and extends northward to the southern Alxa block.

2. Geologic setting

Tectonically, the northeastern Tibetan plateau involves several component blocks to the north of the Jinsha River suture (JRS), including, from south to north, the Songpan–Ganzi (SPGZ), Qaidam–

* Corresponding author. Tel.: +86 10 57909021.
E-mail addresses: ruigao126@126.com, gaorui@cags.ac.cn (R. Gao).

http://dx.doi.org/10.1016/j.epsl.2015.06.024

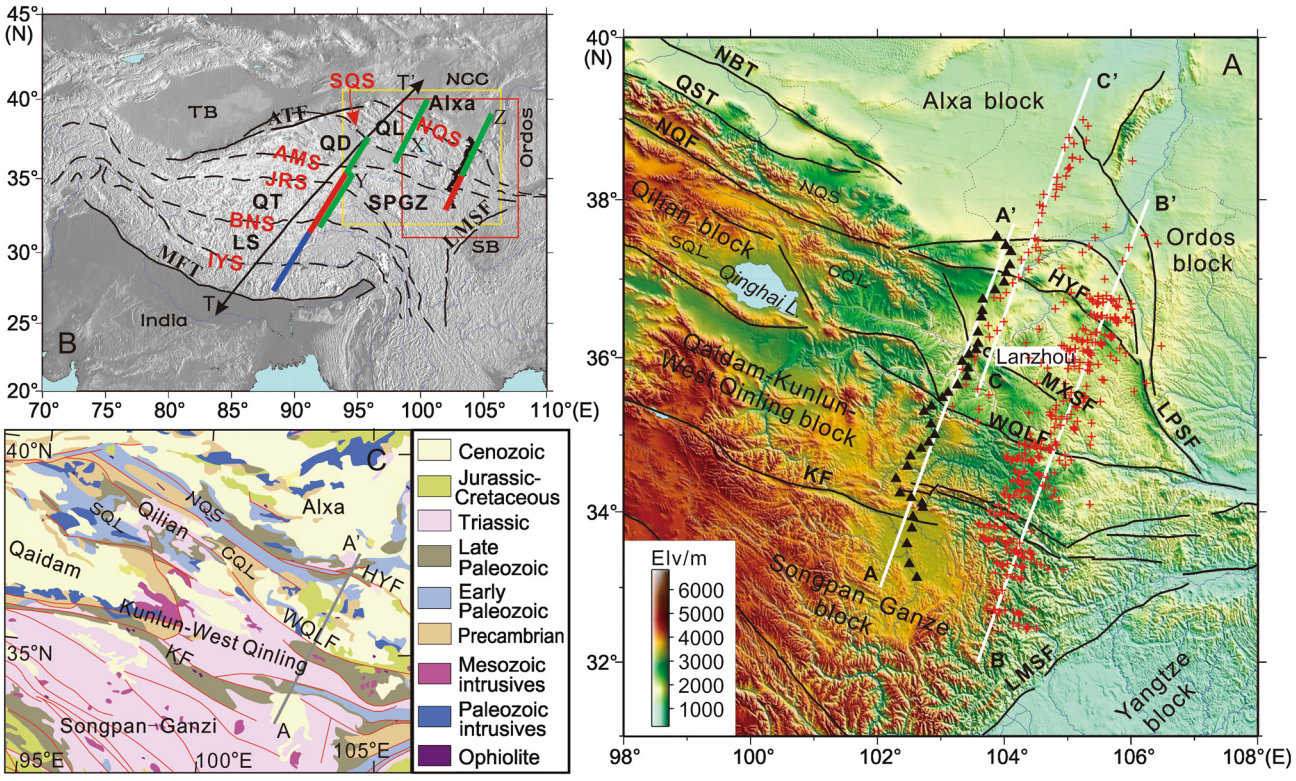

Fig. 1. A: Topographic map of NE Tibet, showing locations of the seismic stations (black triangles). Black solid lines indicate main faults (after Taylor and Yin, 2009). Red crosses show S-to-P conversion points at 150 km depth for involved S-RFs. Solid white lines show P-RF stacking profile (AA') and two S-RF stacking profiles (BB' and CC'). B: Tectonic sketch of the Tibetan plateau. Red and yellow boxes show the map areas of panel A and panel C, respectively. Black triangles mark seismic stations. Bold black bi-direction arrow marks the location of the tomographic transect across Tibet (see Fig. 5D). Colored bars indicate LAB observations: blue = Indian, green = Asian and red = Tibetan LAB, in which X and Y mark previously reported profiles for Tibet (Feng et al., 2014 and Zhao et al., 2011, respectively) and Z marks this study. C: Simplified geologic map of NE Tibet based on the 1:2.5 million scale geologic map of China (Huang et al., 2002) with the gray line indicating our observation profile AA'. Blocks are LS: Lhasa; QT: Qiangtang; SPGZ: Songpan–Ganzi; QD: Qaidam–Kunlun–West Qinling; QL: Qilian (Qilian Shan); NCC: North China craton; TB: Tarim basin; SB: Sichuan basin. IYS: Indus–Yalu suture; BNS: Bangong–Nujiang suture; JRS: Jinsha River suture; AMS: Animaqing suture; SQS: South Qilian suture; NQS: North Qilian suture; MFT: Main frontal thrust; ATF: Altyn-Tagh fault; LMSF: Longmenshan fault; KF: Kunlun fault; WQLF: West Qinling fault; MXSF: Maxianshan fault; HYF: Haiyuan fault; NQF: North Qilian fault; LPSF: Liupanshan fault; QST: Qilian Shan frontal thrust; NBT: North Border thrust (Gao et al., 1999).

Kunlun–West Qinling (QD), Qilian (QL), Alxa and Ordos blocks. NE Tibet is itself bound by the Kunlun fault (KF) system to the south and the Altyn Tagh–Haiyuan fault (ATF–HYF) system to the north. Surrounding NE Tibet are the Alxa and Ordos blocks to the north and northeast, the Tarim basin to the northwest, and the interior Tibetan plateau (Qiangtang and other blocks south) to the south (Fig. 1B).

Thick and pervasively folded Triassic strata, commonly referred to as the Triassic flysch complex (Dewey et al., 1988; Burchfiel et al., 1995; Yin and Harrison, 2000), cover expansive areas of the SPGZ terrane and Kunlun–West Qinling (KL–WQL) ranges, conformably overlying Paleozoic shallow marine sequences of the passive continental margin of North China (Zhou and Graham, 1996) and South China (Burchfiel et al., 1995). The vastly distributed Triassic flysch deposition south of the West Qinling fault (WQLF) is thought to be attributed to the erosion of the WQL orogenic belt in the late Triassic after the SPGZ terrane was accreted to the Qaidam–Kunlun–West Qinling terrane during the late Permian (Dewey et al., 1988; Yin and Nie, 1993; Zhou and Graham, 1993; Yin and Harrison, 2000). Later, the closure of the Animaqing suture (AMS) was completed in the early Jurassic (Dewey et al., 1988). To the north of the WQLF, the Qilian orogen divides (from north to south) into the early Paleozoic North Qilian suture zone (NQS), Central Qilian (CQL) and South Qilian (SQL) belts. Song et al. (2006) suggested that both the Qilian block and the Qaidam block may belong to the same stable Proterozoic "craton" (informally referred to as the Qilian–Qaidam craton) and the Qilian–Qaidam craton collided with the Alxa block when the northward-subducted North Qilian ocean closed along the NQS in the late Ordovician (Yang et al., 2002; Song et al., 2006). The united Qilian orogen is dominated by an imbricate thrust belt (Nan Shan thrust) of Precambrian basement overlain by Paleozoic sedimentary sequences. The Cenozoic Nan Shan thrust belt marks the eastern termination of the ATF system and accommodates shortening along Tibet's northeastern edge (Fig. 1C, Song et al., 2006; Yin and Harrison, 2000).

During the early Cenozoic, shortly after the India–Eurasia collision, the deformation had propagated to NE Tibet (Fang et al., 2003; Duvall et al., 2011), leading to successive reactivation of the old sutures (Gehrels et al., 2003; Ding et al., 2004; Wang et al., 2013) and then crustal shortening/thickening accelerated in NE Tibet during middle to late Miocene (Fang et al., 2005; Lease et al., 2007), which was accompanied by lateral extrusion of continental blocks and controlled by the reactivated strike-slip faults and thrust faults (e.g., the HYF and the KF, Meyer et al., 1998). Using late Mesozoic and Neogene horizons as markers, a minimum of ~150 km of Neogene shortening has been estimated for the region between the northern edge of the Qilian Shan and the KF (Meyer et al., 1998). Based on the amount of left slip along the eastern ATF, Yin and Harrison (2000) inferred that ~340 km of north–south shortening have occurred in the Cenozoic across the Nan Shan thrust belt. Recent geological studies document active NNE–SSW directed crustal shortening along the thrust faults at the northeastern margin of the Qilian Shan at a rate of 1–2 mm/yr over the past 10 Ma (e.g. Zheng et al., 2010; Hetzel, 2013). The Global Positioning System (GPS) measurements

show that the present-day crustal shortening occurs at 5.5 ± 1.5 and 5.5 ± 1.8 mm/yr across NE Tibet perpendicular to the western and eastern Qilian Shan, respectively (Zhang et al., 2004).

3. Data acquisition and receiver functions

The 38 three-component broadband seismograph stations were kept operating continuously for 17 months from October 2011 to March 2013. Each station was equipped with a Guralp 3T/3ESP sensor (32 Guralp 3T and 6 Guralp 3ESP) and a Reftek-130 data acquisition system. This observation profile is oriented NNE with an average station interval of ~15 km (Fig. 1).

P-wave receiver functions (P-RFs) were isolated from seismic records of earthquake events whose magnitudes $Ms \geq 5.5$ and epicentral distances are between 30° and 95°, using time domain iterative deconvolution method (Ligorria and Ammon, 1999). We only rotated the original vertical, north–south and east–west (Z–N–E) components to their station radial-transverse coordinate system (Z–R–T), which is acceptable for P-RF analysis as based on the near-vertical incidence of P-wave (e.g., Rondenay, 2009). Then the P-RFs were extracted from deconvolving the Z component by the R (or T) component. A Gaussian filter parameter $\alpha = 2.5$ was adopted in the deconvolution of the P-RFs, which is capable of detecting crustal structure. We visually inspected each P-RF waveform carefully and picked out the ones that show unambiguous first-order phase *Pms* converted from the Moho and the two related multiple phases *PpPms* and *PpSms* + *PsPms*. Finally we obtained 3765 high-quality P-RFs from all the stations, with 326 earthquakes involved (Supplementary Fig. S1).

S-wave receiver functions (S-RFs) used teleseismic events with $Ms \geq 5.6$ and epicentral distances of 55°–85° and had similar processing procedures applied for the P-RFs. We first rotated the seismic waveforms from their station coordinate system (Z–R–T), which was rotated from the original geographic coordinate system (Z–N–E), to a local ray coordinate system (P–SV–SH) to accommodate the relatively large incident angle of S-wave (Kumar et al., 2006; Zhang et al., 2012a). Then the S-RFs were extracted from deconvolving the P component by the SV component also using the time domain iterative deconvolution (Ligorria and Ammon, 1999). A Gaussian filter parameter $\alpha = 1.0$ was adopted in the deconvolution of the S-RFs (Supplementary Fig. S2).

4. Lithospheric structures beneath NE Tibet

We imaged lithospheric structure beneath NE Tibet using P- and S-RFs subjected to 2-D common conversion point (CCP) migration (e.g., Kosarev et al., 1999; Kind et al., 2002; Kumar et al., 2006). RF cross-sections were obtained by stacking RFs on a vertical plane striking N24°E, a direction roughly perpendicular to the surface trends of major geologic features in NE Tibet.

4.1. Moho observation

We constructed migrations for the direct converted phases *Ps* and its multiple phases *PpPs* (e.g., Kind et al., 2002; Chen et al., 2006; Shen et al., 2014; Ye et al., 2014), respectively. In the *Ps*-migrated images (Fig. 2A), the direct conversions *Ps* (including *Pms* pointing to the Moho) are correctly migrated. In contrary, for the *PpPs*-migrated images (Fig. 2B), the multiple phases *PpPs* (including *PpPms* pointing to the Moho) are correctly migrated as indicators of the true structures, while the direct conversions *Ps* should be mis-positioned. Thanks to the multiple transmissions of the multiple waves in the crust, the converted phases from two closely located interfaces in the Moho are separated from each other, which are probably superposed by each other in the direct conversions (Fig. 2). In receiver function techniques,

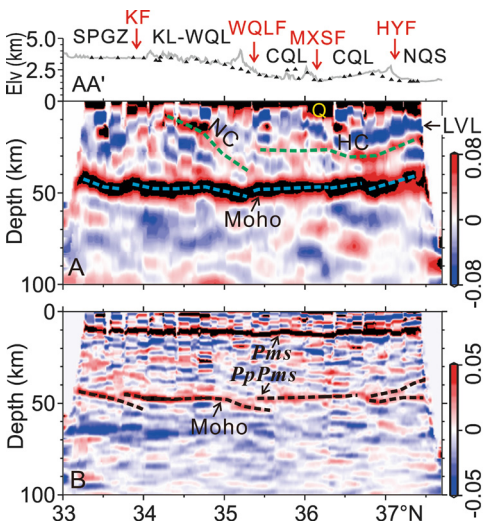

Fig. 2. Migrated P-RF images (0–100 km) along profile AA'. A: *Ps*-migrated and B: *PpPs*-migrated image. Stacking bins are set to be 150 km in width, 2 km along the profile and 0.5 km in depth. Moho and intracrustal converters NC, HC and negative-polarity LVL are marked in panel A. Moho seems finely delineated on the *PpPs*-migrated image (panel B). KL–WQL: Kunlun–West Qinling orogen, CQL: Central Qilian block.

the P and S differential times are used for migration but not absolute travel times, and differential times are more sensitive to the Vp/Vs ratio than to the absolute velocities. Therefore we must take the Vp/Vs ratio variation into consideration when doing the migration of receiver functions (e.g., Kind et al., 2002; Zhang et al., 2014), given that the Vp/Vs ratio variation along our profile herein is fairly large (Fig. 3B). We estimated the crustal Vp/Vs ratio beneath each station by means of the $H - \kappa$ grid-search method (Zhu and Kanamori, 2000). The amplitudes of the converted phase *Pms* from the Moho and its two multiply converted phases *PpPms* and *PpSms* + *PsPms* were summed with the weighting factors of 0.7, 0.2 and 0.1, respectively, to constrain the interference of noise and an average Vp of 6.05 km/s (Zhang et al., 2008) for crust was adopted in the calculation. The average crustal P-wave velocities are relatively low and vary fairly slightly across our study area according to previous wide-angle reflection and refraction (WAR/R) results (Zhang et al., 2008; Jia et al., 2010; Zhang et al., 2013). Thus in the migration imaging, we used the IASP91 earth model of which the crustal part was modified by a laterally variable Vp/Vs ratio adopted from the $H - \kappa$ grid-search results (Fig. 3B), and a variable layering P-wave velocity adapted from previous WAR/R studies (Jia et al., 2010; Zhang et al., 2013).

As the strongest positive feature, the Moho appears clearly as a discontinuity recognizable to a first order and forms a relatively planar surface at an average depth of ~48 km relative to sea level (Fig. 2A). The Moho exhibits offset (e.g., ~5 km offset beneath the KF, WQLF and HYF) and a degree of overlap (e.g., ~10–20 km horizontal overlap beneath the KF and WQLF zones and ~50 km horizontal overlap beneath the NQS zone) beneath fault zones between blocks, particularly in the *PpPs*-migrated image (Fig. 2B). The Moho overlap was also observed at the western segment of the KF zone across the southern margin of Qaidam basin by Zhu and Helmberger (1998), Shi et al. (2009) and WAR/R profiling of Karplus et al. (2011). Du et al. (2011) observed similar features of Moho overlap beneath the NQS zone. RF migrations with the effect of lateral variation of crustal Vp/Vs ratios considered yield reliable evidence of the Moho and clearly define its topography. The Moho depth variations either estimated from grid-search method or defined by migration for direct converted phases *Ps* or multiple phases *PpPs* have fairly good consis-

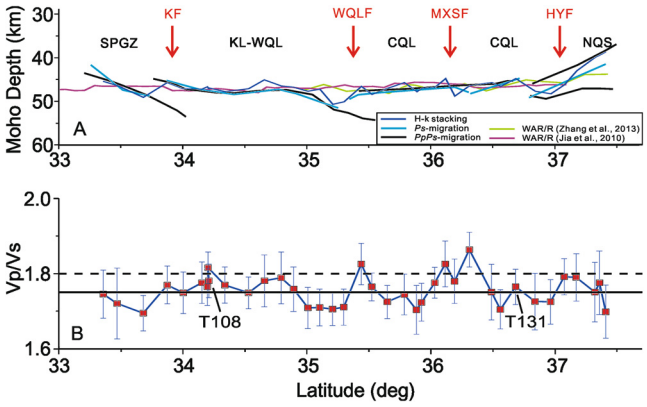

Fig. 3. Crustal Vp/Vs ratio and Moho topography. A: Moho identifications from different methods. The Moho topography generated from each method is consistent with each other and coincides with WAR/R results (for locations of the WAR/R seismic profiles, see lines 1 and 2 in Fig. 6A), with the lateral variation of Vp/Vs ratio considered in the migration. B: Crustal Vp/Vs ratios along profile AA' estimated from grid-search method. The red filled squares represent the best estimated Vp/Vs ratios with one standard deviation indicated by the error bars. The dashed line indicates 1.80 level and solid line 1.75.

tency (Fig. 3A). Beneath the NQS north of ~36.8° N, the double Moho is well delineated by *PpPms* phase while the *Pms* phase only obtains a general Moho. The Moho interfaces delineated by two WAR/R profiles (profiles 1 and 2 in Fig. 6A, Zhang et al., 2013; Jia et al., 2010) located in close proximity to our profile AA' is coincident with our result (Fig. 3A).

The complex Moho structures underlying fault zones between blocks also appear in P-RF traces of individual stations located within fault zones. P-RF traces of two stations, T119 and T138, which are respectively located at the WQLF zone and the HYF zone, are presented here (Fig. 4). The double-pulse Moho conversion is observed for waves coming at 150–250° back-azimuth in both the *Ps* and *PpPs* migrated P-RF traces of T138 (Figs. 4B and 4C), with the two pulses separated by ~12 km. The fact that the Moho double pulses have amplitudes comparable to each other and appear in both *Ps* and *PpPs* migrated P-RF traces essentially rules out the possibility of reverberations. The *Ps* and *PpPs* migrated P-RF traces of T119 present a very complex Moho conversion between back-azimuthal range of 50–200°, with the double pulses appearing within some back-azimuthal ranges, e.g., 50–100° and 150–200° (Figs. 4D and 4E). This kind of complex Moho conversion with double pulses is probably associated with waveform effects (diffraction) caused by a sharp Moho offset and a small amount of overlap by the Qilian Moho above the lowermost KL–WQL crust may be involved in (e.g., Zhu and Helmberger, 1998; Shi et al., 2009).

4.2. Intracrustal features

Several intracrustal converters that appear in raw P-RF data (Supplementary Fig. S1.A) are labeled with green dashed lines in Fig. 2A. One converter (NC), begins at ~10 km depth and dips steeply to the north, descending through most of the crustal section beneath the WQL orogen, and then merging with the lower crust beneath the WQLF zone (Fig. 2A). Another feature is a subhorizontal converter (HC) that forms a relatively planar feature throughout the lower crust beneath the CQL and NQS. A negative-polarity intracrustal converter is interpreted to represent the upper surface of a lower velocity layer (LVL) at the base of the upper crust beneath the CQL and NQS. This LVL, deepening slightly from north to south, can be traced smoothly and continuously to areas north of the Maxianshan fault. It gradually becomes obscure towards the south beneath the highland (Fig. 2A).

4.3. LAB observation

S-RF stacking was performed along profiles BB' and CC', which were positioned according to the surface distribution of S-to-P conversion points (Fig. 1A). The S-to-P conversion points were parsed into two groups by only obtaining good S-RFs adequate for stacking at two rather narrow back-azimuthal windows (Supplementary Fig. S1.B). Profile BB' is located ~150 km to the southeast of the P-RF stacking profile AA', while CC' lies in close proximity to AA'. Profile CC' extends across the NQS and further northward into the interior of the Alxa block. The same velocity model as for the P-RFs is used here for S-RF migration. The Moho signals obtained from S-RFs at depth as well as other patterns are consistent with those observed in P-RF images. A negative signal beneath the Moho is clearly evident in S-RF images (marked as black dashed lines in Figs. 5A and 5B). We interpret this negative phase at around 100–200 km depth as representing the lithosphere–asthenosphere boundary (LAB). On the BB' profile, the LAB gradually deepens from ~100 km at the southern edge of the section to ~125 km beneath the AMS. It persists in a sub-horizontal orientation north to the WQLF, where it shifts to a depth of ~150 km. North of this drop, the LAB maintains a sub-horizontal orientation relative to the northern section of the profile. The LAB can be traced continuously along the CC' profile, where it dips southward from ~120 km depth beneath the interior of the Alxa block to ~160 km depth beneath the Qilian orogen.

Despite the presence of crustal multiples, the SRF-LAB is relatively consistent with some negative phase areas of the subsurface (meaning decreasing velocity with depth and probably not artifacts of multiples) imaged beneath the Moho by the P-RFs (Fig. 5C). Zhang et al. (2010) reported similar features in S-RF images of areas beneath the eastern SPGZ block and identified the LAB at analogous depths of ~100 km. The LAB interface identified in this study is robustly observable in both high and low frequency data (Supplementary Fig. S2), verifying that it is not an artifact of high-frequency scattering from vertical heterogeneities. Moreover, comprehensive seismic images across central and western areas of the NCC (Chen et al., 2014 and references therein) reveal an intralithospheric discontinuity at 80–100 km depth beneath the Ordos block, which has a thick cratonic keel extending down to ~200 km depth; but there is no presence of this intralithospheric feature beneath the Qilian orogen or Alxa block, which are underlain by a relatively thin lithosphere of 100–140 km. The above observations support the interpretation that the negative anomaly observed at 100–150 km depth beneath the study area represents the LAB rather than an intralithospheric discontinuity.

Replumaz et al. (2013) presented a body wave tomographic image of the entire Tibetan plateau, which is shown in Fig. 5D along with LAB observations from Zhao et al. (2011) and this study. The positive anomaly indicative of the Indian plate (IP) bends in a manner consistent with LAB trends shown in Zhao et al. (2011) (white dashed line in Fig. 5D). Beneath north–central Tibet, the positive anomalies indicative of the Qaidam (QP) and North China plates (NCP) dip to the south and accord with LAB observations for the QP and NCP mantle lithosphere (black dashed lines in Fig. 5D, also see Zhao et al., 2011).

5. Discussion

5.1. Comparisons/combinations with previous profiling studies across NE Tibet

We reviewed data and interpretations from previous profiling studies of NE Tibet in the vicinity of our profile. The NC and LVL crustal features appearing in the P-RF image presented here are consistent with other regional subsurface seismic features

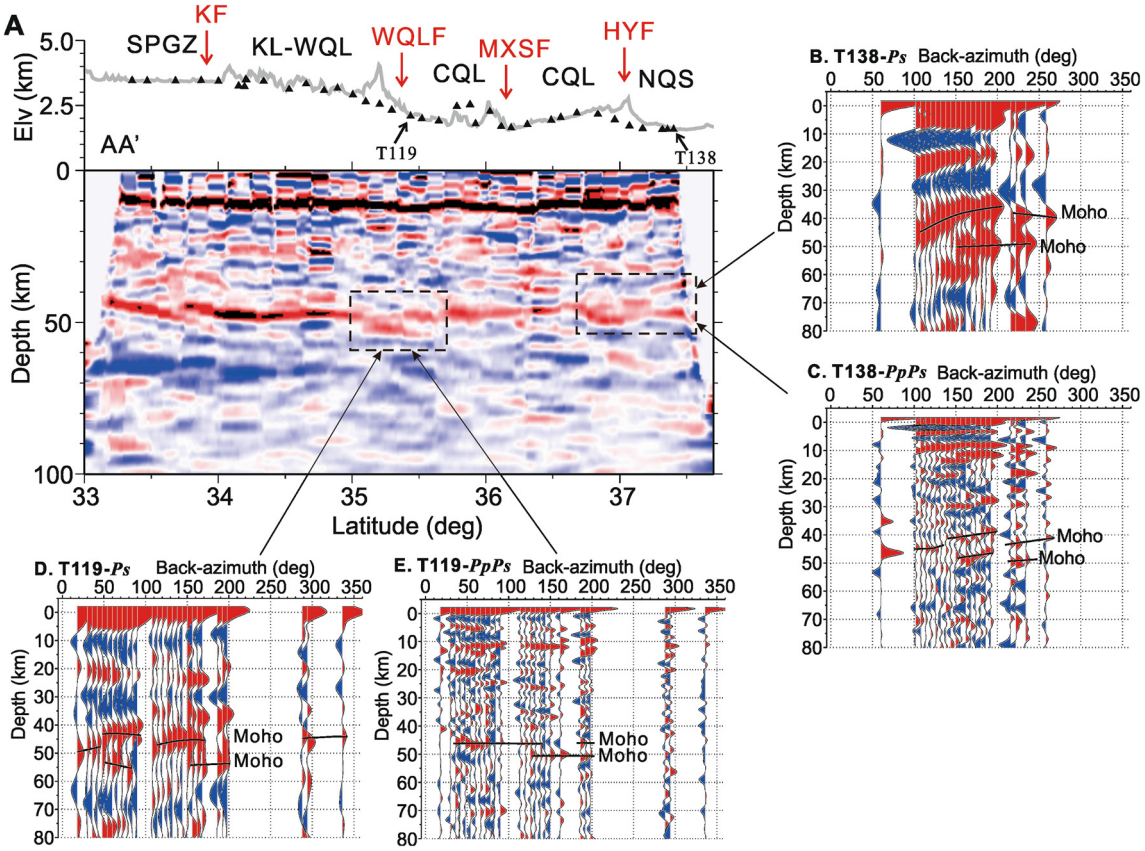

Fig. 4. Complex Moho structures at the junctions between blocks. Dashed rectangular boxes on the *PpPs*-migrated image along profile AA' (panel A) outline the complex Moho beneath the WQLF zone and the HYF zone. *Ps*- and *PpPs*-migrated P-RF traces sorted by back azimuths for two stations T138 (panels B and C) and T119 (panels D and E) are shown as representatives of the complex Moho at the two junctions. P-RF traces are stacked in 6° back-azimuth.

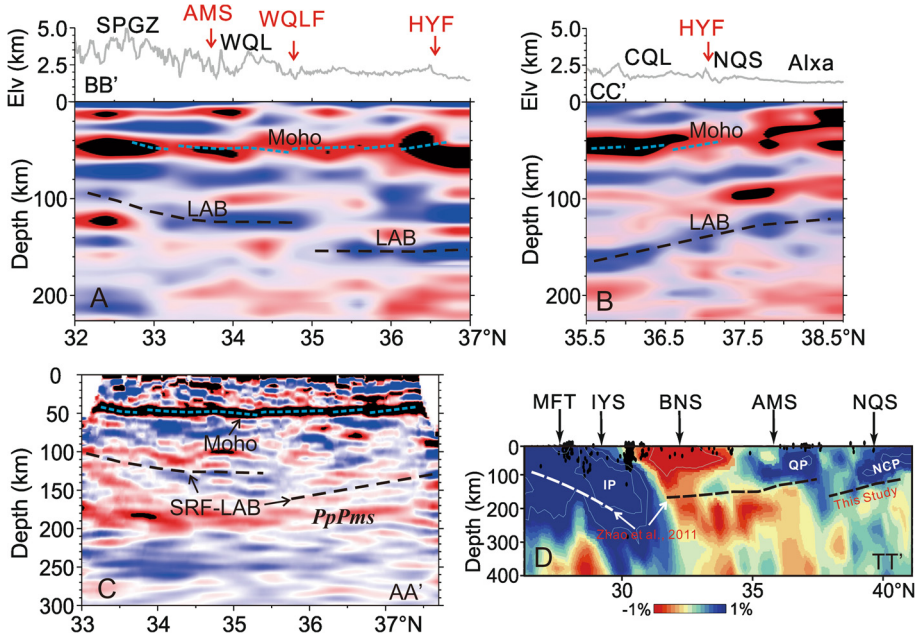

Fig. 5. S receiver functions (S-RFs) imaging the LAB. A: and B: Migrated S-RF images along respective BB' and CC' profiles. Stacking bins are set as 160 km in width, 60 km in length and a moving step of 45 km along the profile. The LAB is marked by black dashed lines. The Moho from P-RF imaging in Fig. 2A is plotted on S-RF images for comparison (light blue dashed lines). C: Migrated P-RF image for a depth range of 0–300 km along profile AA', with the LAB from S-RF images plotted (black dashed lines) for comparison. D: A tomographic image from a transect across Tibet (Replumaz et al., 2013, see Fig. 1B for location). LAB observations from Zhao et al. (2011) and this study (white and black dashed lines, respectively) are projected on the cross-section. IP, QP and NCP refer to the Indian, Qaidam and North China plates, respectively.

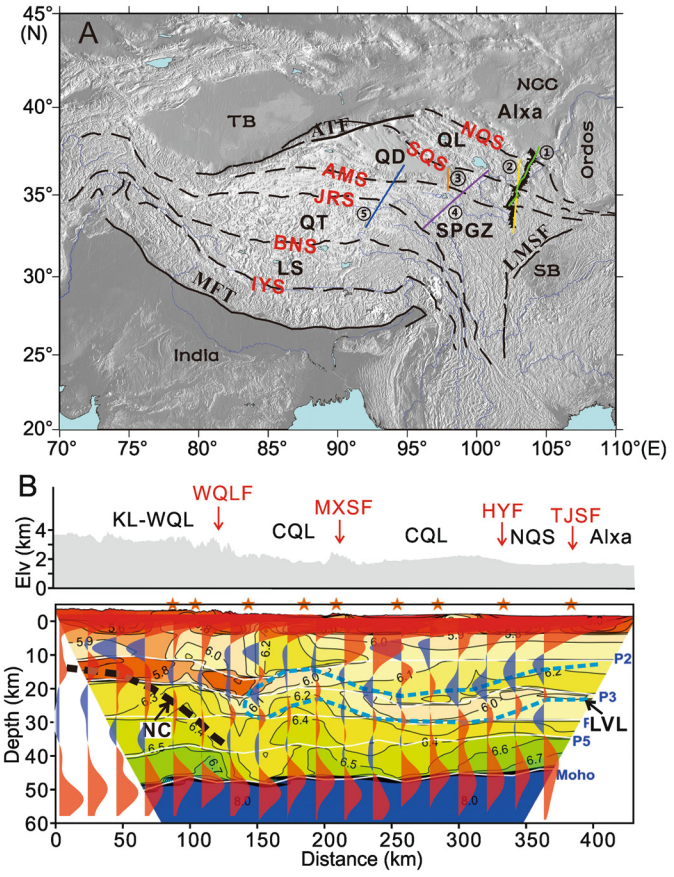

Fig. 6. A: Locations of several previous seismic profiles (1: WAR/R, Zhang et al., 2013; 2: WAR/R, Jia et al., 2010; 3: broadband, Shi et al., 2009; 4 and 5: broadband, Vergne et al., 2002). Black triangles represent our seismic stations. B: Comparison between the Jingtai–Hezuo WAR/R velocity model (Zhang et al., 2013, superposing our profile AA', line 1 in panel A) and our receiver function observation. The bin-stacked P-RF traces along profile AA' are projected onto the WAR/R section. Stacking bins are set as 150 km in width and 30 km in length, with a moving step of 20 km along the profile. Thick-black and blue-dashed lines respectively delineated the NC and LVL features defined from receiver functions.

(Figs. 6 and 7). The NC feature defined by the receiver functions (black dashed line in Fig. 6B) coincides well with the north-deepening velocity jump interface on the Jingtai–Hezuo WAR/R velocity model (for location see profile 1 in Fig. 6A, Zhang et al., 2013). The LVL feature as observed in our receiver functions is also clearly presented on the WAR/R velocity model roughly coincident with our observation (outlined with blue dashed line in Fig. 6B). The WAR/R velocity model shows that the upper crustal velocities fall precipitously while the lower crust is relatively uniform from the CQL to the WQL orogen across the WQLF (Fig. 6B). These observations suggest that upper crustal deformation may be decoupled from the underlying crust, which could be attributed to the LVL at the base of the upper crust. This LVL beneath the Qilian orogen was also identified by ambient noise tomography observations of Bao et al. (2013) and Li et al. (2014) and was interpreted to be associated with partial melting/fluids in the crust. Therefore, the observed LVL herein could be a mechanically weak zone beneath the Qilian orogen (Bao et al., 2013) that facilitates the crustal decoupling. But this LVL could not be reckoned as an unequivocal evidence for the middle/lower crustal channel flow (e.g., Royden et al., 1997, 2008) because it has a relatively higher shear wave velocity (3.3–3.5 km/s) and thus perhaps a higher viscosity, compared to the LVLs in other parts of Tibet (e.g., the SPGZ block) (Bao et al., 2013; Li et al., 2014), and is also too thin to allow vigorous flow.

The NC features can also be laterally comparable to those observed by counterpart profiles that traverse the KL–WQL orogen west of the study region. We depicted at a unified scale the main crustal features identified from these previous broadband seismic profiles, thus to do direct comparisons between them (Fig. 7). The NC features defined by these experiments have similar patterns in shape and scale, dipping in a low angle of about 20–25° (on average) to the north. We therefore interpret the NC as a dominant crustal feature of the KL–WQL orogen that indicates a south-directed thrust system predominantly occurring in the upper crust (indicating upper crustal thickening, Tian and Zhang, 2013; Xu et al., 2014). In addition, deep seismic reflection surveys revealed north-directed imbricate thrusts in the upper crust beneath the WQL and Qilian orogens (red markers in Fig. 8). These subordinate structures may accommodate the major sinistral strike slip faults, e.g., the WQLF, HYF and TJSF as well as the active thrust faults, e.g., the NBT (Gao et al., 1999, 2013, 2014; Wang et al., 2013; Wang et al., 2014).

5.2. A comprehensive lithospheric model

Based on receiver function images and previously published geophysical information on NE Tibet (e.g., Zhao et al., 2011; Replumaz et al., 2013; Feng et al., 2014), we constructed a comprehensive lithospheric model of the study area (Fig. 8). Rayleigh wave tomography indicates a warm and weak lithosphere (above ~100–130 km depth) characterized by low shear wave velocity south of the WQLF. A relatively cold and rigid lithosphere resides north of this fault however, as evident from high shear wave velocity (e.g., Yu et al., 2014; Li et al., 2013). The southward dipping LAB (Fig. 5B) may indicate southward underthrusting of the Alxa's cold mantle lithosphere under the Qilian orogen in response to compression between the interior Tibetan plateau and the NCC (Fig. 8). Tomographic imaging has outlined underthrusting slabs of the Asian continental plate beneath north–central Tibet, which also supports our interpretations (Fig. 5D). Our receiver functions imply that the leading edge of the NCC's underthrusting mantle lithosphere may reach the southern margin of the Qilian orogen, while recent profiling to the west of our profile suggests it may extend further south (line X in Fig. 1B, Feng et al., 2014). South of the Qilian orogen, the INDEPTH profiling (located southwest of our profile, line Y in Fig. 1B, Zhao et al., 2011) across the Qaidam basin indicates that the Qaidam lithosphere may have underthrust further southward beyond the BNS in central Tibet, consistent with tomographic observations (Fig. 5D). The images presented here, combined with previous information, suggest stepwise subduction of Asian lithospheric blocks beneath the Tibetan plateau (Fig. 8). Additionally, it should be mentioned that the asthenosphere may branch from its eastward flow beneath central and eastern Tibet to flow northeastward as it encounters the rigid barrier of the Sichuan basin. This asthenospheric flow may contribute to the relatively thin lithosphere observed beneath the eastern SPGZ and WQL orogen, through attenuation or delamination effects (Zhang et al., 2010). In contrast, the rigid cratonic lithosphere beneath the Qilian orogen was not so easily attenuated by asthenospheric flow, and thus retains a thicker mantle lithosphere.

5.3. Tectonic implications

Combining our observations with the idea of stepwise subduction of Asian lithospheric blocks, we attempt to clarify the tectonic evolution of NE Tibet. Large Paleozoic sutures such as the SQS and NQS were reactivated in the Cenozoic in response to the India–Asia collision at ~55 Ma and thus the weakly assembled Asian lithosphere was sheared anew along major strike-slip faults (Peltzer and Tapponnier, 1988; Meyer et al., 1998; Gehrels et al., 2003; Ding et al., 2004; Wang et al., 2013), which probably have caused offset/overlap observed in the Moho and strong anisotropy in

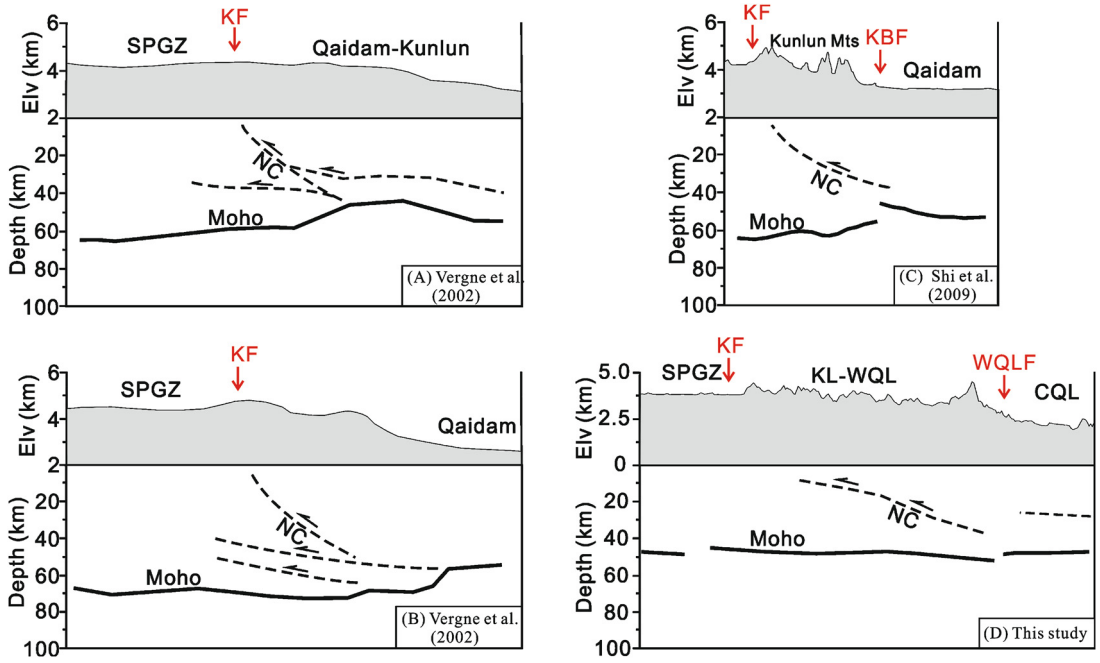

Fig. 7. Structural sketches based on several broadband seismic profiles across the Qaidam–Kunlun–West Qinling terrane, with the vertical and horizontal axes expressed at the same scale. Only the most noticeable signals, here, i.e. the Moho and the intracrustal north-dipping converters (NC), are delineated by bold black lines and dashed black lines, respectively. Interpretations of the converters are referred to Wang et al. (2011). For the locations of these sections, see Fig. 6A: (A) part of profile 4; (B) part of profile 5; (C) profile 3; KBF: Kunlun Border fault; (D) part of our profile AA'.

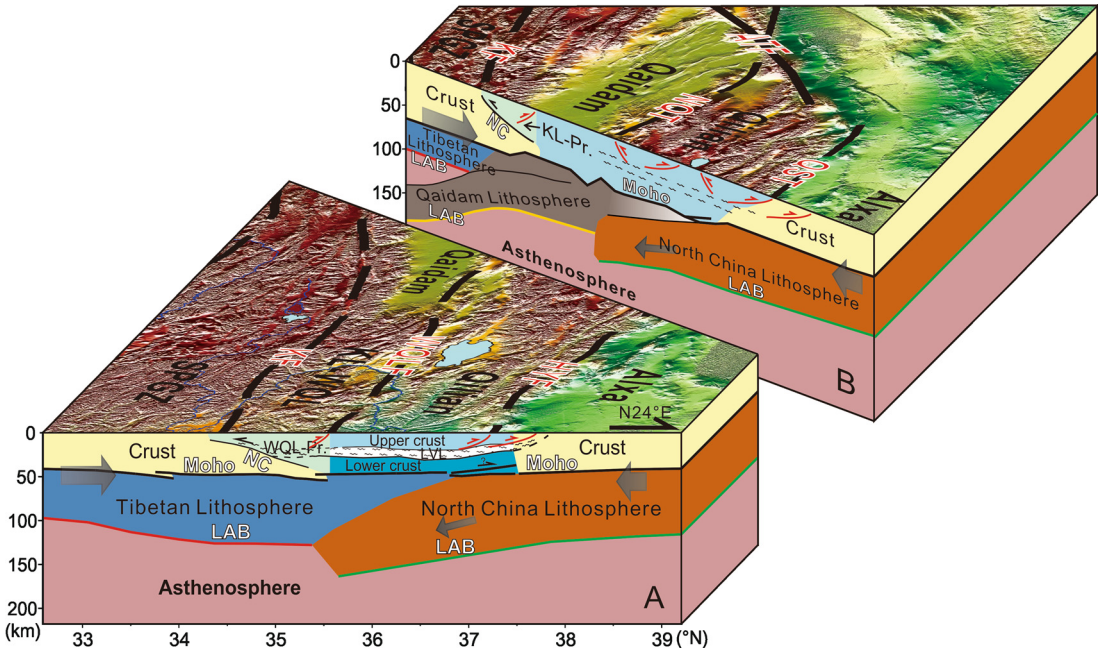

Fig. 8. A comprehensive lithospheric model of northeastern Tibetan plateau including structural features inferred from receiver function imaging. Section A is based on our results and section B is synthesized from Feng et al. (2014) and Zhao et al. (2011) (profiles X and Y in Fig. 1B). The vertical and horizontal axes are shown at the same scale. While sub-horizontal crustal layering beneath the Qilian orogen is well delineated, detailed intracrustal structures beneath the SPGZ and Alxa blocks are not shown here due to ambiguities of imaging. WQL-Pr: West Qinling orogenic prism, KL-Pr: Kunlun orogenic prism.

boundary zones between blocks (Figs. 2 and 4, remarkable increase of SKS-wave splitting time in the vicinities of fault zones, Ye et al., under review). Subsequently, oblique mantle subduction of Asian plates (Fig. 8) was successively triggered (Tapponnier et al., 1990; Meyer et al., 1998). The initiation of the KF at 15–8 Ma (Fu and Awata, 2007; Jolivet et al., 2003) indicates the roughly coeval lithospheric subduction of the Qaidam–Kunlun block along this fault in Neogene. Then following that subduction, the NCC mantle lithosphere may have begun to subduct southward. The reactivation timing of the HYF indicates subduction beginning by late Miocene time (Meyer et al., 1998; Wang et al., 2013). Since then, the NCC lithospheric mantle has been persistently underthrust beneath the Qilian orogen in response to on-going convergence between NE Tibet and the NCC. Coevally, successive accretion of thick-skinned crustal wedges above a mid- to lower-crustal decollement generates crustal shortening and thickening (Tapponnier et al., 1990; Gaudemer et al., 1995; Meyer et al., 1998). Features like the NC and the gently southward dipping LVL indicate crust-level thrusts

and extrusions developed from accretionary wedges. Paleozoic Qilian and Triassic KL–WQL strata both exhibit pervasive deformation and outward thrusting by accretionary prisms (Fig. 8) with the LVL serving as an intracrustal decollement. This process resulted in pronounced uplift of the Qilian and KL–WQL ranges. Here we suggest the observed underthrusting is an on-going phenomena initiated by Cenozoic collisional event rather than a previous subduction event, assumed to occur in the early Paleozoic, following the closure of the NQS. This inference derives from two compelling lines of evidence: (1) most of the crustal shortening between the northern edge of the Qilian orogen and the KF may have occurred and still occurring during the Cenozoic (Meyer et al., 1998; Zheng et al., 2010; Hetzel, 2013; Zhang et al., 2004) and (2) the absence of major tectonic events in the study area since the closure of the NQS, save for the Cenozoic India–Asia collision (Yin and Harrison, 2000; Gehrels et al., 2003).

6. Conclusions

Our observations provide key geophysical constraints on lithospheric deformation affecting NE Tibet that may refine regional tectonic models. Seismic images indicate mantle underthrusting of the NCC plate beneath the Qilian orogen. This process contributes to formation of syntectonic crustal accretionary wedges, which evolved above a mid- to lower-intracrustal decollement. Pure shear shortening would be mainly dominated at a crustal scale with considerable extrusion and thrust activities. Overall, our observations, combined with previous seismic imaging, can be well accommodated in a model of northeastward migration of stepwise mantle subduction that facilitates plateau growth in a crustal-wedge manner in NE Tibet (e.g., Tapponnier et al., 1990, 2001).

Acknowledgements

We are grateful to the Earthquake Administration of Gansu Province for their generous assistance with the field work. We thank Dr. Xiaoyu Guo and two anonymous reviewers for constructive comments and suggestions. This work was supported by Sinoprobe02 (grant 201011042) and the National Natural Science Foundation of China (grants 40830316, 41174081 and 41104034).

Appendix A. Supplementary material

Supplementary material related to this article can be found online at http://dx.doi.org/10.1016/j.epsl.2015.06.024.

References

Bao, X., Song, X., Xu, M., Wang, L., Sun, X., Mi, N., 2013. Crust and upper mantle structure of the North China craton and the NE Tibetan Plateau and its tectonic implications. Earth Planet. Sci. Lett. 369, 129–137.

Burchfiel, B.C., Chen, Z., Liu, Y., Royden, L.H., 1995. Tectonics of the Longmen Shan and adjacent regions, central China. Int. Geol. Rev. 37, 661–735.

Ceylan, S., Ni, J., Chen, J.Y., Zhang, Q., Tilmann, F., Sandvol, E., 2012. Fragmented Indian plate and vertically coherent deformation beneath eastern Tibet. J. Geophys. Res. 117, B11303. http://dx.doi.org/10.1029/2012JB009210.

Chen, L., Jiang, M., Yang, J., Wei, Z., Liu, C., Ling, Y., 2014. Presence of an intralithospheric discontinuity in the central and western North China craton: implications for destruction of the craton. Geology 42, 223–226.

Chen, L., Zheng, T., Xu, W., 2006. Receiver function migration image of the deep structure in the Bohai Bay Basin, eastern China. Geophys. Res. Lett. 33, L20307. http://dx.doi.org/10.1029/2006GL027593.

Dewey, J.F., Shackelton, R.M., Chang, C., Sun, Y., 1988. The tectonic evolution of the Tibetan Plateau. Philos. Trans. R. Soc. Lond. A 327, 379–413.

Ding, G., Chen, J., Tian, Q., Shen, X., Xing, C., Wei, K., 2004. Active faults and magnitudes of left-lateral displacement along the northern margin of the Tibetan Plateau. Tectonophysics 380, 243–260.

Du, Y., Sandvol, E., Shi, D., Li, H., Li, X., Li, A., Yue, H., Shen, Y., 2011. S-wave receiver function study in northeast Tibet and adjacent boundaries. In: AGU 2011 Fall Meeting (abstract #S31E-2282).

Duvall, A.R., Clark, M.K., van der Pluijm, B.A., Li, C.Y., 2011. Direct dating of Eocene reverse faulting in northeastern Tibet using Ar-dating of fault clays and low-temperature thermochronometry. Earth Planet. Sci. Lett. 304, 520–526.

Fang, X., Garzione, C., Van der Voo, R., Li, J., Fan, M., 2003. Flexural subsidence by 29 Ma on the NE edge of the Tibet from the magnetostratigraphy of the Linxia basin, China. Earth Planet. Sci. Lett. 210, 545–560.

Fang, X., Yan, M., Van der Voo, R., Rea, D.K., Song, C., Parés, J.M., Gao, J., Nie, J., Dai, S., 2005. Late Cenozoic deformation and uplift of the NE Tibetan Plateau: evidence from high-resolution magnetostratigraphy of the Guide Basin, Qinghai Province, China. Geol. Soc. Am. Bull. 117, 1208–1225.

Feng, M., Kumar, P., Mechie, J., Zhao, W., Kind, R., Su, H., Xue, G., Shi, D., Qian, H., 2014. Structure of the crust and mantle down to 700 km depth beneath the East Qaidam basin and Qilian Shan from P and S receiver functions. Geophys. J. Int. 199, 1416–1429.

Fu, B., Awata, Y., 2007. Displacement and timing of left-lateral faulting in the Kunlun Fault Zone, northern Tibet, inferred from geologic and geomorphic features. J. Asian Earth Sci. 29, 253–265.

Gao, R., Cheng, X., Wu, G., 1999. Lithospheric structure and geodynamic model of the Golmud–Ejin transect in northern Tibet. In: Macfarlane, A., Sorkhabi, R.B., Quade, J. (Eds.), Himalaya and Tibet: Mountain Roots to Mountain Tops. In: Geol. Soc. Am. Spec. Pap., vol. 328, pp. 9–17.

Gao, R., Wang, H., Yin, A., Dong, S., Kuang, Z., Zuza, A.V., Li, W., Xiong, X., 2013. Tectonic development of the northeastern Tibetan Plateau as constrained by high-resolution deep seismic-reflection data. Lithosphere 5, 555–574. http://dx.doi.org/10.1130/L293.1.

Gao, R., Wang, H., Zeng, L., Zhang, J., Guo, T., Li, Q., Li, W., Li, P., Guan, Y., 2014. The crust structures and the connection of the Songpan block and West Qinling orogen revealed by the Hezuo–Tangke deep seismic reflection profiling. Tectonophysics 634, 227–236.

Gaudemer, Y., Tapponnier, P., Meyer, B., Peltzer, G., Shunmin, G., Zhitai, C., Huagung, D., Cifuentes, I., 1995. Partitioning of crustal slip between linked, active faults in the eastern Qilian Shan, and evidence for a major seismic gap, the 'Tianzhu gap', on the western Haiyuan Fault, Gansu (China). Geophys. J. Int. 120, 599–645.

Gehrels, G.E., Yin, A., Wang, X.F., 2003. Detrital-zircon geochronology of the northeastern Tibetan plateau. Geol. Soc. Am. Bull. 115, 881–896.

Hetzel, R., 2013. Active faulting, mountain growth, and erosion at the margins of the Tibetan Plateau constrained by in situ-produced cosmogenic nuclides. Tectonophysics 582, 1–24.

Huang, C., Ye, T., Chen, K., Wu, K., 2002. Geological map of China (1:2,500,000). China Geological Survey. China Cartographic Publishing House, Beijing, China.

Jia, S., Zhang, X., Zhao, J., 2010. Deep seismic sounding data reveals the crustal structures beneath Zoige basin and its surrounding folded orogenic belts. Sci. China, Ser. D, Earth Sci. 39, 203–212.

Jolivet, M., Brunel, M., Seward, D., Xu, Z., Yang, J., Malavieille, J., Roger, F., Leyreloup, A., Arnaud, N., Wu, C., 2003. Neogene extension and volcanism in the Kunlun Fault Zone, northern Tibet: new constraints on the age of the Kunlun Fault. Tectonics 22, 1052. http://dx.doi.org/10.1029/2002TC001428.

Karplus, M.S., Zhao, W., Klemperer, S.L., Wu, Z., Mechie, J., Shi, D., Brown, L.D., Chen, C., 2011. Injection of Tibetan crust beneath the south Qaidam Basin: evidence from INDEPTH IV wide-angle seismic data. J. Geophys. Res. 116, B07301. http://dx.doi.org/10.1029/2010JB007911.

Kind, R., Yuan, X., Saul, J., Nelson, D., Sobolev, S.V., Mechie, J., Zhao, W., Kosarev, G., Ni, J., Achauer, U., Jiang, M., 2002. Seismic images of crust and upper mantle beneath Tibet: evidence for Eurasian plate subduction. Science 298, 1219–1221.

Kosarev, G., Kind, R., Sobolev, S.V., Yuan, X., Hanka, W., Oreshin, S., 1999. Seismic evidence for a detached Indian lithospheric mantle beneath Tibet. Science 283, 1306–1309.

Kumar, P., Yuan, X.H., Kind, R., Ni, J., 2006. Imaging the collision of the Indian and Asian Continental Lithospheres Beneath Tibet. J. Geophys. Res. 111, B06308. http://dx.doi.org/10.1029/2005JB003930.

Lease, R.O., Burbank, D.W., Gehrels, G.E., Wang, Z.C., Yuan, D.Y., 2007. Signatures of mountain building: detrital zircon U/Pb ages from northeastern Tibet. Geology 35, 239–242.

Li, H., Shen, Y., Huang, Z., Li, X., Gong, M., Shi, D., Sandvol, E., Li, A., 2014. The distribution of the mid-to-lower crustal low-velocity zone beneath the northeastern Tibetan Plateau revealed from ambient noise tomography. J. Geophys. Res. 119. http://dx.doi.org/10.1002/2013JB010374.

Li, L., Li, A., Shen, Y., Sandvol, E.A., Shi, D., Li, H., Li, X., 2013. Shear wave structure in the northeastern Tibetan Plateau from Rayleigh wave tomography. J. Geophys. Res. 118, 4170–4183.

Liang, X., Sandvol, E., Chen, Y.J., Hearn, T., Ni, J., Klemperer, S., Shen, Y., Tilmann, F., 2012. A complex Tibetan upper mantle: a fragmented Indian slab and no south-verging subduction of Eurasian lithosphere. Earth Planet. Sci. Lett. 333, 101–111.

Ligorria, J.P., Ammon, C.J., 1999. Iterative deconvolution and receiver-function estimation. Bull. Seismol. Soc. Am. 89, 1395–1400.

Meyer, B., Tapponnier, P., Bourjot, L., Metivier, F., Gaudemer, Y., Peltzer, G., Shunmin, G., Zhitai, C., 1998. Crustal thickening in Gansu–Qinghai, lithospheric mantle subduction, and oblique, strike-slip controlled growth of the Tibet plateau. Geophys. J. Int. 35, 1–47.

Nabelek, J., György, H., Vergne, J., Sapkota, S., Kafle, B., Jiang, M., Su, H., Chen, J., Huang, B.S., Hi-CLIMB Team, 2009. Underplating in the Himalaya–Tibet collision zone revealed by the Hi-CLIMB experiment. Science 325, 1371–1374.

Peltzer, G., Tapponnier, P., 1988. Formation and evolution of strike-slip faults, rifts, and basins during India–Asia collision: an experimental approach. J. Geophys. Res. 93, 15085–15117.

Replumaz, A., Guillot, S., Villaseñor, A., Negredo, A.M., 2013. Amount of Asian lithospheric mantle subducted during the India/Asia collision. Gondwana Res. 24, 936–945.

Rondenay, S., 2009. Upper mantle imaging with array recordings of converted and scattered teleseismic waves. Surv. Geophys. 30, 377–405.

Royden, L.H., Burchfiel, B.C., King, R.W., Wang, E., Chen, Z., Shen, F., Yuping, L., 1997. Surface deformation and lower crustal flow in eastern Tibet. Science 276, 788–790.

Royden, L.H., Burchfiel, B.C., van der Hilst, R.D., 2008. The geological evolution of the Tibetan plateau. Science 321, 1054–1058.

Shen, X., Zhou, Y., Zhang, Y., Mei, X., Guo, X., Liu, X., Qin, M., Wei, C., Li, C., 2014. Receiver function structures beneath the deep large faults in the northeastern margin of the Tibetan Plateau. Tectonophysics 610, 63–73.

Shi, D., Shen, Y., Zhao, W., Li, A., 2009. Seismic evidence for a Moho offset and southdirected thrust at the easternmost Qaidam–Kunlun boundary in the Northeast Tibetan plateau. Earth Planet. Sci. Lett. 288, 329–334.

Song, S., Zhang, L., Niu, Y., Su, L., Song, B., Liu, D., 2006. Evolution from oceanic subduction to continental collision: a case study of the northern Tibetan Plateau inferred from geochemical and geochronological data. J. Petrol. 47, 435–455.

Tapponnier, P., Meyer, B., Avouac, J.P., Peltzer, G., Gaudemer, Y., Shunmin, G., Hongfa, X., Kelun, Y., Zhitai, C., Shuahua, C., Huagang, D., 1990. Active thrusting and folding in the Qilian Shan, and decoupling between upper crust and mantle in northeastern Tibet. Earth Planet. Sci. Lett. 97, 382–403.

Tapponnier, P., Xu, Z., Roger, F., Meyer, B., Arnaud, N., Wittlinger, G., Yang, J., 2001. Oblique stepwise rise growth of the Tibet plateau. Science 294, 1671–1677.

Taylor, M.H., Yin, A., 2009. Active faulting on the Tibetan Plateau and sounding regions relationships to earthquakes, contemporary strain, and late Cenozoic volcanism. Geosphere 5, 199–214.

Tian, X., Zhang, Z., 2013. Bulk crustal properties in NE Tibet and their implications for deformation model. Gondwana Res. 24, 548–559.

Vergne, J., Wittlinger, G., Qiang, H., Tapponnier, P., Poupinet, G., Jiang, M., Paul, A., 2002. Seismic evidence for step-wise thickening of the crust across the NE Tibetan Plateau. Earth Planet. Sci. Lett. 203, 25–33.

Wang, C., Gao, R., Yin, A., Wang, H., 2011. A mid-crustal strain-transfer model for continental deformation: a new perspective from high-resolution deep seismic reflection profiling across NE Tibet. Earth Planet. Sci. Lett. 306, 279–288.

Wang, H., Gao, R., Zeng, L., Kuang, Z., Xue, A., Li, W., Xiong, X., Huang, W., 2014. Crustal structure and Moho geometry of the northeastern Tibetan plateau as revealed by SinoProbe-02 deep seismic-reflection profiling. Tectonophysics 636, 32–39.

Wang, W., Kirby, E., Zhang, P., Zheng, D., Zhang, G., Zhang, H., Zheng, W., Chai, C., 2013. Tertiary basin evolution along the northeastern margin of the Tibetan Plateau: evidence for basin formation during Oligocene transtension. Geol. Soc. Am. Bull. 125, 377–400.

Xu, T., Wu, Z., Zhang, Z., Tian, X., Deng, Y., Wu, C., Teng, J., 2014. Crustal structure across the Kunlun fault from passive source seismic profiling in East Tibet. Tectonophysics 627, 98–107.

Yang, J., Xu, Z., Zhang, J., Song, S., Shi, R., Wu, C., Li, H., Brunel, M., 2002. Early Paleozoic North Qaidam UHP metamorphic belt on the north-eastern Tibetan Plateau and a paired subduction model. Terra Nova 14, 397–404.

Ye, Z., Li, Q., Gao, R., Zhang, H., He, R., Wang, H., Li, W., 2014. A thinned lithosphere beneath coastal area of southeastern China as evidenced by seismic receiver functions. Sci. China, Ser. D, Earth Sci. 57, 2835–2844.

Yin, A., Harrison, T.M., 2000. Geological evolution of the Himalayan–Tibetan orogen. Annu. Rev. Earth Planet. Sci. 28, 211–280.

Yin, A., Nie, S., 1993. An indentation model for North and South China collision and the development of the Tanlu and Honam fault systems, eastern Asia. Tectonics 12, 801–813.

Yu, D., Li, Y., Wu, Q., Pan, J., Zhang, F., He, J., 2014. S-wave velocity structure of the northeastern Tibetan Plateau from joint inversion of Rayleigh wave phase and group velocities. Chin. J. Geophys. 57, 800–811.

Yue, H., Chen, Y.J., Sandvol, E., Ni, J., Hearn, T., 2012. Lithospheric and upper mantle structure of the northeastern Tibetan Plateau. J. Geophys. Res. 117, B05307. http://dx.doi.org/10.1029/2011JB008545.

Zhang, H., Teng, J., Tian, X., Zhang, Z., Gao, R., Liu, J., 2012a. Lithospheric thickness and upper mantle deformation beneath the NE Tibetan plateau inferred from S receiver functions and SKS splitting measurements. Geophys. J. Int. 191, 1285–1294.

Zhang, H., Zhao, D., Zhao, J., Xu, Q., 2012b. Convergence of the Indian and Eurasian plates under eastern Tibet revealed by seismic tomography. Geochem. Geophys. Geosyst. 13, Q06W14. http://dx.doi.org/10.1029/2012GC004031.

Zhang, P., Shen, Z., Wang, M., Gan, W., Bürgmann, R., Molnar, P., Wang, Q., Niu, Z., Sun, J., Wu, J., Sun, H., You, X., 2004. Continuous deformation of the Tibetan Plateau from global positioning system data. Geology 32, 809–812.

Zhang, X., Jia, S., Zhao, J., 2008. Crustal structures beneath West Qinling–East Kunlun orogen and its adjacent area—results of wide-angle seismic reflection and refraction experiment. Chin. J. Geophys. 51, 439–450 (in Chinese).

Zhang, Z., Bai, Z., Klemperer, S.L., Tian, X., Xu, T., Chen, Y., Teng, J., 2013. Crustal structure across northeastern Tibet from wide-angle seismic profiling: constraints on the Caledonian Qilian orogeny and its reactivation. Tectonophysics 606, 140–159.

Zhang, Z., Wang, Y., Houseman, G.A., Xu, T., Wu, Z., Yuan, X., Teng, J., 2014. The Moho beneath western Tibet: shear zones and eclogitization in the lower crust. Earth Planet. Sci. Lett. 408, 370–377.

Zhang, Z., Yuan, X., Chen, Y., Tian, X., Kind, R., Li, X., Teng, J., 2010. Seismic signature of the collision between the east Tibetan escape flow and the Sichuan Basin. Earth Planet. Sci. Lett. 292, 254–264. http://dx.doi.org/10.1016/j.epsl.2010.01.046.

Zhao, J., Yuan, X., Liu, H., Kumar, P., Pei, S., Kind, R., Zhang, Z., Teng, J., Ding, L., Gao, X., Xu, Q., Wang, W., 2010. The boundary between the Indian and Asian tectonic plates below Tibet. Proc. Natl. Acad. Sci. USA 107, 11229–11233.

Zhao, W., Kumar, P., Project INDEPTH Team, 2011. Tibetan plate overriding the Asian plate in central and northern Tibet. Nat. Geosci. 4, 870–873.

Zheng, D., Clark, M.K., Zhang, P., Zheng, W., Farley, K.A., 2010. Erosion, fault initiation and topographic growth of the North Qilian Shan (northern Tibetan Plateau). Geosphere 6, 937–941.

Zhou, D., Graham, S.A., 1993. Songpan–Ganzi Triassic flysch complex as a remnant-ocean-basin along diachronous collision orogen, central China. Abstr. Program – Geol. Soc. Am. 25, A118.

Zhou, D., Graham, S.A., 1996. The Songpan–Ganzi complex of the western Qinling Shan as a Triassic remnant ocean basin. In: Yin, A., Harrison, T.M. (Eds.), The Tectonic Evolution of Asia. Cambridge Univ. Press, Cambridge, UK, pp. 281–299.

Zhu, L., Helmberger, D.V., 1998. Moho offset across the northern margin of the Tibetan Plateau. Science 281, 1170–1172.

Zhu, L., Kanamori, H., 2000. Moho depth variation in southern California from teleseismic receiver functions. J. Geophys. Res. 105, 2969–2980.